Editors' Suggestion

High-pressure behavior of the magnetic van der Waals molecular framework $Ni(NCS)_2$

Madeleine Geers,[1,2] David M. Jarvis,[3] Cheng Liu,[3] Siddharth S. Saxena,[3] Jem Pitcairn,[1] Emily Myatt,[1] Sebastian A. Hallweger,[4] Silva M. Kronawitter,[4] Gregor Kieslich,[4] Sanliang Ling,[5] Andrew B. Cairns,[6] Dominik Daisenberger,[7] Oscar Fabelo,[2] Laura Cañadillas-Delgado,[2,*] and Matthew J. Cliffe[1,†]

[1]*School of Chemistry, University Park, University of Nottingham, Nottingham NG7 2RD, United Kingdom*
[2]*Institut Laue Langevin, 71 avenue des Martyrs CS 20156, 38042 Grenoble Cedex 9, France*
[3]*Cavendish Laboratory, University of Cambridge, Cambridge CB3 0HE, United Kingdom*
[4]*TUM Natural School of Sciences, Technical University of Munich, D-85748 Garching, Germany*
[5]*Advanced Materials Research Group, Faculty of Engineering, University of Nottingham, University Park, Nottingham NG7 2RD, United Kingdom*
[6]*Department of Materials, Imperial College London, Royal School of Mines, Exhibition Road, London SW7 2AZ, United Kingdom*
[7]*Diamond Light Source, Chilton, Didcot OX11 0DE, United Kingdom*

(Received 7 August 2023; revised 22 September 2023; accepted 28 September 2023; published 31 October 2023)

Two-dimensional materials offer a unique range of magnetic, electronic, and mechanical properties which can be controlled by external stimuli. Pressure is a particularly important stimulus, as it can be achieved readily and can produce large responses, especially in low-dimensional materials. In this paper, we explore the pressure dependence of the structural and magnetic properties of a two-dimensional van der Waals (vdW) molecular framework antiferromagnet with ferromagnetic layers, $Ni(NCS)_2$, up to 8.4 kbar. Through a combination of x-ray and neutron diffraction analysis, we find that $Ni(NCS)_2$ is significantly more compressible than comparable vdW metal halides, and its response is anisotropic not only out of the plane, but also within the layers. Using bulk magnetization and neutron diffraction data, we show that the ambient layered antiferromagnetic phase is maintained up to the largest investigated pressure, but with an enhanced Néel temperature, T_N ($\Delta T_N/T_N = +19\%$), and a large pressure sensitivity ($Q = \frac{1}{T_N}\frac{dT_N}{dP} = +2.3\%\,\text{kbar}^{-1}$), one of the larger values of magnetic pressure responsiveness for a vdW material. Density functional theory calculations suggest that this is due to increasing three dimensionality. These results provide insights into the pressure response of molecular framework vdW magnets and suggest that the investigation of other molecular framework vdW magnets might uncover contenders for future pressure-switchable devices.

DOI: 10.1103/PhysRevB.108.144439

I. INTRODUCTION

Magnetic van der Waals (vdW) materials, compounds formed from two-dimensional layers held together through weak dispersion interactions, have been the subject of much recent interest as potential single-layer magnetic materials capable of being embedded in spintronic devices [1]. The weak interactions between layers means pressure can switch the sign of interactions, for example, bilayer CrI_3 undergoes an antiferromagnetic-ferromagnetic transition at 27 kbar [2]. It can also induce large enhancements of magnetic interactions, e.g., the ordering temperature T_c increases by 250 K in $FeCl_2$ with the application of 420 kbar ($Q = \frac{1}{T_c}\frac{dT_c}{dP} = +2.4\%\,\text{kbar}^{-1}$) [3], and in NiI_2, T_c increases by 230 K when compressed to 190 kbar ($Q = +1.6\%\,\text{kbar}^{-1}$) [4], as well an enhancement of the helimagnetic state [5,6]. Pressure can also induce qualitative changes in the electronic structure of vdW magnets [7], such as pressure-induced metal-insulator transitions [8,9]. NiI_2 undergoes a pressure-induced metal-insulator transition at 190 kbar [4], as does the recently reported vdW antiferromagnet $FePS_3$ at 140 kbar [10]. Pressure can even induce superconductivity in $FePSe_3$ above 90 kbar [11].

Molecular frameworks, made from metals and molecular ligands, have inherently higher flexibility than nonmolecular materials comprised of only atomic ions. The increased length of the ligands enhances the extent of flexing of the frameworks [12,13]. They therefore can be expected to produce large responses at pressures closer to those realizable in practical devices. For example, the magnetic ordering temperature of the three-dimensional cyanide frameworks, $[Mn(4\text{-dmap})]_3[Mn(CN)_6]_2$ (4-dmap = 4-dimethylaminopyridine) ($Q = +13\%\,\text{kbar}^{-1}$) [14] and $[Ru_2(O_2CCH_3)_4]_3[Cr(CN)_6]$ ($Q = +6.5\%\,\text{kbar}^{-1}$) [15], rapidly increase with pressure. Our understanding of the pressure response of the magnetism of vdW molecular framework magnets is rapidly developing [16–18].

Nickel(II) thiocyanate, $Ni(NCS)_2$, is a binary pseudohalide and the only member of the $M(NCS)_2$ family (M = Mn, Co, Fe, Ni, Cu) thus far reported to have in-layer ferromagnetism

*canadillas-delgado@ill.fr
†matthew.cliffe@nottingham.ac.uk

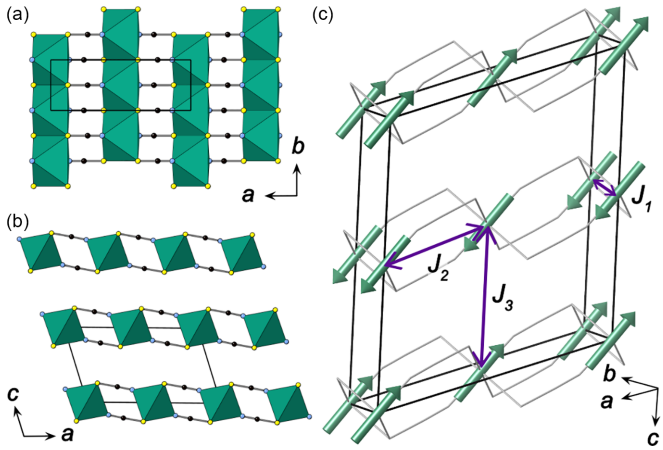

FIG. 1. Structure of $Ni(NCS)_2$ adapted from Ref. [17]: (a) in-plane structure, (b) layer stacking. Ni = green octahedra, N = blue, C = black, S = yellow. (c) The magnetic structure with the three nearest-neighbor interactions identified. The $Ni(NCS)_2$ framework is shown as a wire frame for clarity.

[17,19–21] (Néel temperature, $T_N = 54$ K; cf. $NiBr_2$ $T_N = 52$ K [22]), and is predicted to be a single-layer ferromagnet [23]. It adopts an analogous structure to that of the two-dimensional transition-metal halides MX_2, comprising NiS_4N_2 octahedra which edge share to form layers in the *ab* plane (Fig. 1), which stack along the *c* direction. The rod shape and directionality of the NCS^- lowers the symmetry from the rhombohedral symmetry of NiX_2 to the monoclinic space group $C2/m$ [17]. This relieves the potential frustration and means that no helimagnetic state is found, unlike $NiBr_2$ and NiI_2 [22].

Here we report the structural and magnetic changes of $Ni(NCS)_2$ as it is compressed to pressures up to 8.4 kbar. X-ray and neutron powder diffraction experiments have allowed us to follow the evolution of both lattice parameters and the structure under compression. Our combination of magnetometry and low-temperature neutron diffraction measurements show the enhancement of the magnetic ordering temperature with pressure and confirm the magnetic ground state throughout. We carry out density functional theory (DFT) calculations which explain the energetic origins of the observed behavior.

II. METHODS

A. Synthesis

The synthesis of the samples of $Ni(NCS)_2$ was carried out following the reported synthetic method of Bassey *et al.* [17]. A typical synthesis (quantities as for the neutron sample) is described below.

$NiSO_4 \cdot 6H_2O$ (16.56 g, 63 mmol) was dissolved in deionized H_2O (50 mL), giving a clear green solution. An aqueous solution of $Ba(SCN)_2 \cdot 3H_2O$ (19.37 g, 63 mmol, 120 mL) was added, with the rapid formation of a white precipitate and a green solution. The reaction mixture was stirred at room temperature overnight and the precipitate was removed by centrifugation and filtering under reduced pressure. The solution was removed *in vacuo*, giving a green-brown microcrystalline powder of $Ni(NCS)_2$. The compound is stable to humidity in the investigated conditions.

B. Magnetic measurements

Measurements of the magnetic susceptibility were carried out on a pelletized powder sample of $Ni(NCS)_2$ using a Quantum Design Magnetic Property Measurements System (MPMS) 3 Superconducting Quantum Interference Device (SQUID) magnetometer with moment measurements carried out in direct current (DC) mode. The measured data were collected at pressures of 1.2, 3.8, 5.2, and 8.4 kbar. The zero-field-cooled (ZFC) susceptibility was measured in an applied field of 0.01 T over the temperature range 2 to 300 K. The pressure was applied using a BeCu piston cylinder pressure cell from CamCool Research Ltd., with a Daphne 7373 oil pressure medium. A small piece of Pb was included in the sample space to act as a pressure gauge [24]. As $M(H)$ is linear in this field regime, the small-field approximation for the susceptibility, $\chi(T) \simeq \frac{M}{H}$, where M is the magnetization and H is the magnetic field intensity, was taken to be valid. Isothermal magnetization measurements were carried out on the same sample at 10 K over the field range -7 to $+7$ T for each pressure point.

C. DFT

We have performed density functional theory calculations to probe the structures and energetics of the spin order of $Ni(NCS)_2$. The spin-polarized DFT + U method (with Grimme's D3 van der Waals correction [25]) was employed in the structural optimizations and energy calculations, using the Vienna Ab initio Simulation Package (VASP) [26]. In our DFT + U calculations, we used a U value of 5.1 eV for the d electrons of Ni^{2+} cations [27,28], and a range of ferromagnetic and antiferromagnetic spin solutions were considered for magnetic Ni^{2+} cations (see Table 2 in the Supplemental Material [29]). We used a plane-wave basis set with a kinetic energy cutoff of 520 eV to expand the wave functions. The Perdew-Burke-Ernzerhof functional [30] in combination with the projector augmented wave method [31,32] was used to solve the Kohn-Sham equations. An energy convergence threshold of 10^{-6} eV was used for electronic energy minimization calculations, and the structural optimizations, including cell parameters and atomic positions, were considered converged if all interatomic forces fell below 0.01 eV/Å. All DFT calculations have been performed in the primitive cell (two formula units per cell) using a k grid with a k-point spacing of around 0.1 $Å^{-1}$. To improve the accuracy of the three nearest-neighbor magnetic interactions determined from DFT calculations at different pressures, we additionally performed single-point DFT energy calculations of the various spin configurations at the optimized structures with a higher plane-wave cutoff energy of 800 eV. We note that the relative energy difference between several spin configurations in our DFT calculations can be less than 1 meV/metal (depending on pressure), which is close to the DFT accuracy that we can achieve with our current computational settings.

D. Synchrotron diffraction measurements

X-ray powder diffraction experiments were performed at beamline I15 at the Diamond Light Source, UK, with a wavelength of $\lambda = 0.4246$ Å, applying a custom-made high-pressure powder x-ray diffraction setup suitable for measurements up to 4 kbar [33]. A powder sample of $Ni(NCS)_2$ was filled into a soft plastic capillary together with silicone oil AP-100 as a nonpenetrating pressure-transmitting medium to maintain hydrostatic conditions. The capillaries were sealed with Araldyte-2014-1. The capillary was loaded into, and in direct contact with, the sample chamber consisting of a metal block filled with water. The water acts as a pressure-transmitting medium, controlled with a hydraulic gauge pump.

Constant wavelength powder x-ray diffraction data were collected at room temperature in the pressure range 0.001 to 4 kbar with a step of 0.2 kbar and an estimated error of ±0.0030 bar. The data were processed using DAWN [34] with a LaB_6 calibration. Rietveld refinements of the nuclear model were completed using the FULLPROF program [35] and strain analysis carried out using PASCal [36].

E. Neutron diffraction measurements

1. High-resolution measurements (D2b)

Constant wavelength neutron powder diffraction data were collected on the high-resolution D2b diffractometer [37] at the Institut Laue Langevin (ILL), France. The incident wavelength was $\lambda = 1.59$ Å and the scattering was measured over an angular range of $10 < 2\theta < 160°$. The sample was loaded in an aluminium holder and placed within an aluminium gas pressure cell with helium used as a pressure-transmitting medium. Diffraction data were collected at room temperature with applied pressures of 1.7, 3.4, 5.1, and 6.7 kbar, with an estimated error of ±0.5 kbar. Further diffraction data were collected at a pressure of 6.7 kbar at temperatures of 20, 40, and 180 K. The pressure was set at room temperature, then the system was cooled for the low-temperature data. The cell was operated with a gas compressor to regulate the pressure as the temperature was lowered and ensure maintenance of constant pressure. A heater inside the gas capillary ensured the helium was gaseous at low temperatures. NOMAD software [38] from the ILL was used for data collection. Refinements of the nuclear models were completed using the FULLPROF program [35].

2. High-intensity measurements (D1b)

Constant wavelength powder neutron diffraction data were collected on the high-intensity medium resolution D1b diffractometer [39] at the Institut Laue Langevin (ILL), France. The incident wavelength was $\lambda = 2.52$ Å and the scattering was measured over an angular range of $2 < 2\theta < 128°$. The sample was loaded in an aluminium holder and placed within an aluminium gas pressure cell with helium used as a pressure-transmitting medium. Diffraction data were collected at room temperature with applied pressures of 3, 4.5, and 6.7 kbar, with an estimated error of ±0.5 kbar. A thermal diffractogram was collected at 3 kbar, heated with a programmed ramp of 0.05 K min^{-1} between 34 and 65 K. A second thermal diffractogram was collected at 4.5 kbar, heated with a programmed ramp of 0.07 K min^{-1} between 44 and 60 K. At a pressure of 6.7 kbar, data were collected at a constant temperature of 20 K. The pressure was set at room temperature, then the system was cooled for the low-temperature data. The cell was operated with a gas compressor to regulate the pressure as the temperature was lowered and ensure maintenance of constant pressure. A heater inside the gas capillary ensured the helium was gaseous at low temperatures. NOMAD software [38] from the ILL was used for data collection. Refinements of the nuclear and magnetic model were completed using the FULLPROF program [35].

III. RESULTS

The structural and magnetic changes that $Ni(NCS)_2$ undergo with temperature at ambient pressure have previously been determined by Bassey *et al.* [17]. The compound crystallizes in the monoclinic $C2/m$ space group as two-dimensional layers stacked along the c axis. It has an ambient magnetic ordering temperature, T_N^0, of 54 K, below which it magnetically orders as an antiferromagnet. The moments correlate ferromagnetically within the ab plane and antiferromagnetically between adjacent planes, ordering with a propagation vector of $\mathbf{k}= (0, 0, \frac{1}{2})$ in the magnetic space group C_c2/c. The moments are oriented along the N-Ni-N bond direction and are restricted to the ac plane by symmetry. The three nearest-neighbor interactions are J_1 through Ni-S-Ni (b direction), J_2 along Ni-NCS-Ni (a direction), and J_3 occurs between the metals on adjacent layers [c direction; Fig. 1(c)].

A. Nuclear structure under pressure

Ambient temperature diffraction measurements were carried out on a powder sample of $Ni(NCS)_2$ using x rays (I15, Diamond, UK) between 0.001 and 4.0 kbar (in 0.2 kbar steps) and with neutrons (D2b, ILL, France) at 1.7, 3.4, 5.1, and 6.7 kbar. The variation in lattice parameters was determined by performing Rietveld refinements for both the x-ray and neutron data (Fig. 2). The atom positions and anisotropic displacement parameters were fixed to that of the structure at ambient pressure [17]. Throughout the refinements, the lattice parameters were refined freely, along with background and peak shape parameters. From these analyses, we found no evidence of a phase transition, with $Ni(NCS)_2$ retaining its monoclinic symmetry throughout the pressure regime. From refinements of the x-ray data, the volume is reduced from 225.18(6) $Å^3$ at 0.001 kbar to 220.65(6) $Å^3$ at 4.0 kbar. Fitting the x-ray data to a third-order Birch-Murnaghan equation of state [40] gives a bulk modulus $B_0 = 170(2)$ kbar and $B' = 15(1)$. Comparable trends are observed for the compressibilities and reduction in axes observed for the neutron data up to 6.7 kbar as well [$B_0 = 156(6)$ kbar and $B' = 22(3)$; Fig. 3].

Both data sets, x ray and neutron, show that as $Ni(NCS)_2$ is compressed, all unit cell axes decrease in length, while the β angle remains broadly constant (Fig. 3). To assess the degree of anisotropy, the strains along the principal axes were calculated (Table I) using the PASCal program [36]. The principal axes X_1, X_2, and X_3 lie in the following directions: $X_1 \approx a$, along the Ni-NCS-Ni pathway; $X_2 = b$, along the Ni-S-Ni

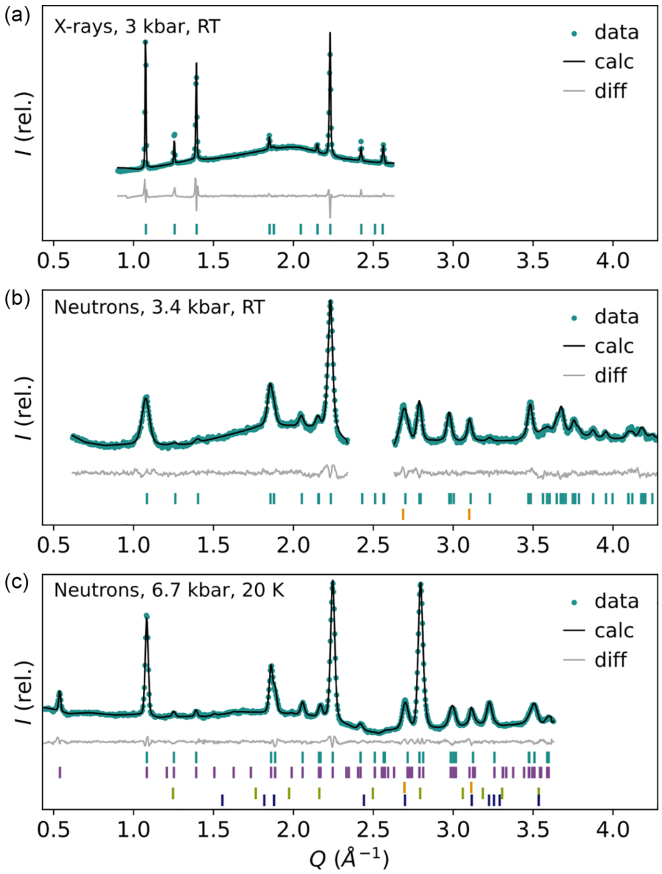

FIG. 2. Rietveld refinements of diffraction data. (a) Synchrotron x-ray data (I15, Diamond) measured at 3 kbar and at ambient temperature, (b) neutron data (D2b, ILL) measured at 3.4 kbar and at ambient temperature, (c) neutron data (D1b, ILL) measured at 6.7 kbar and at 20 K. Le Bail fits were made to account for reflections arising from the aluminium, oxygen, and nitrogen. The tick marks show the position of structural reflections (turquoise), magnetic reflections (purple), the aluminium sample holder (orange), oxygen (light-green) and nitrogen (dark-blue) phases.

bonds; $X_3 \approx c$, between the layers. The pressure dependence of the principal axes shows that the compressibilities, $K_i = -1/\varepsilon_i \frac{d\varepsilon_i}{dP}$, derived from fitting an empirical equation of state $[\varepsilon_i(P) = \varepsilon_0 + \lambda(P - P_C)^v]$, are very anisotropic. $K_3 = 32.5(3)$ TPa^{-1} is more than double $K_2 = 13.5(1)$ TPa^{-1}, and $K_1 = 3.8(4)$ TPa^{-1} is an order of magnitude smaller.

TABLE I. Compressibilities (K) for the principle axes of $Ni(NCS)_2$ calculated from synchrotron x-ray data (I15, Diamond) at 4 kbar and from neutron data (D2b, ILL) at 6.7 kbar. The definition of the principal axes (X_i) is given relative to the unit cell (a, b, c) for the structure at 4 kbar.

	K (TPa^{-1})				
Axes	X-rays	Neutrons	a	b	c
X_1	3.8(4)	3(2)	0.990	0.0	0.141
X_2	13.5(1)	13.9(8)	0.0	1.0	0.0
X_3	32.5(2)	26.9(6)	0.124	0.0	0.992
V	50.0(5)	48(1)			

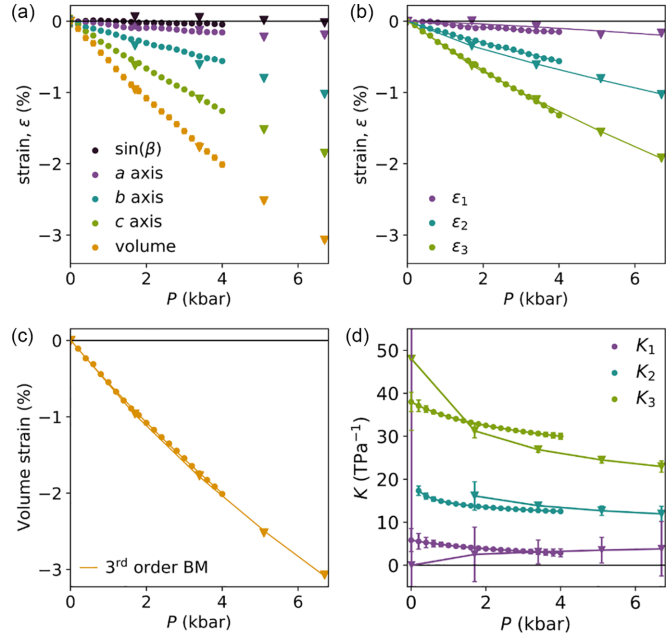

FIG. 3. Crystallographic parameter variations determined from Rietveld refinements at ambient temperature using x rays (circles, measured with I15, Diamond, 0.001 to 4 kbar) and neutrons (triangles, measured with D2b, ILL, 0.001 to 6.7 kbar). (a) Normalized change of the unit cell parameters. (b) Strain (ε_i) along the principal axes (X_i) with lines showing the linear compressibilities. (c) The volume dependence with pressure, fitted with the third-order Birch-Murnaghan (BM) equation of state with $B_0 = 170(2)$ kbar and $B' = 15(1)$ at 4 kbar for x rays and $B_0 = 156(6)$ kbar and $B' = 22(3)$ at 6.7 kbar for neutrons. (d) The compressibility (K) along the principal axes as a function of pressure. Standard errors are shown with vertical lines.

To explore the changes in the structure over a broader pressure range, DFT calculations were performed at nominal pressures of 0, 5, 10, 20, 50, and 100 kbar. These calculations, as they were carried out at 0 K, were in the experimentally derived layered antiferromagnetic ground state. The fitted bulk modulus using the third-order Birch-Murnaghan equation of state is 255.7(2) kbar, with $B' = 6.42(9)$. The compressibilities at 10 kbar are $K_3 = 18.1(5)$ TPa^{-1}, $K_2 = 10.1(4)$ TPa^{-1}, and $K_1 = 3.0(2)$ TPa^{-1}, broadly consistent with the measured compressibilities. On increasing the pressure to 100 kbar, we find, as expected, a significant stiffening: $K_3 = 5.1(5)$ TPa^{-1}, $K_2 = 5.5(8)$ TPa^{-1}, and $K_1 = 1.9(5)$ TPa^{-1}.

B. Variable-temperature high pressure

We also sought to investigate the effect of high pressure on the thermal expansion of this material by measuring variable-temperature neutron diffraction patterns ($T = 20$, 40, 180, and 298 K) at our maximum pressure of 6.7 kbar. We find normal volumetric thermal expansion, with a coefficient of thermal expansion $\alpha_V = 1/V \frac{dV}{dT} = 42(3)$ MK^{-1}. At 6.7 kbar, the thermal expansion is anisotropic with linear thermal expansivities along the principal strain directions of $\alpha_1 = 1/\varepsilon_1 \frac{d\varepsilon_1}{dT} = 26(1)$ MK^{-1}, $\alpha_2 = 14(2)$ MK^{-1}, and $\alpha_3 = 1.12(5)$ MK^{-1} [broadly in the same directions as the compressibilities; Fig. 4(a)]. There are also significant

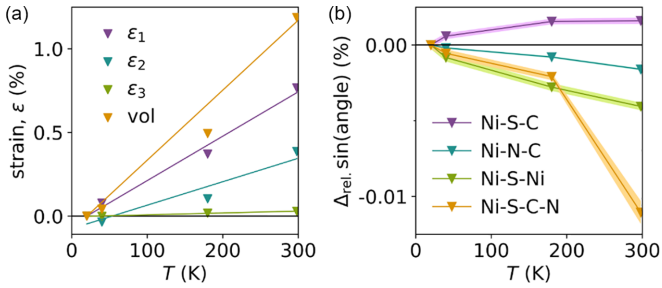

FIG. 4. Selected data from Rietveld refinements at 6.7 kbar measured at 20, 40, 180, and 298 K using the D2b diffractometer (ILL). (a) Relative change in the principle axes and volume, (b) relative change in sin(angle) of Ni-ligand bonds and the dihedral angle Ni-S-C-N. The shaded regions show the calculated errors.

structural changes: with ∠Ni-S-Ni (along X_2) expanding significantly on cooling, $\Delta\sin(\text{Ni-S-Ni}) = -0.0041(2)\%$, whereas ∠Ni-N-C and ∠Ni-S-C (predominantly along X_1) change much less, $\Delta\sin(\text{Ni-N-C}) = -0.00160(6)\%$ and $\Delta\sin(\text{Ni-S-C}) = +0.0016(2)\%$. The torsion angle between Ni-S-C-N decreases by $\Delta\sin(\text{Ni-N-C}) = -0.0111(7)\%$ [Fig. 4(b)].

At this highest pressure of 6.7 kbar, additional peaks emerged in the neutron datasets at high Q at temperatures below approximately 55 K, which is well into the magnetic ordered phase. These likely arise from a combination of oxygen and/or nitrogen phases crystallizing due to the presence of air in the pressure cell, and we accounted for them using additional Le Bail phases [41,42]. We found no anomalies in the magnetometry data corresponding to this transition, further supporting our assumption that this is not sample related.

C. Magnetometry

To assess how the bulk magnetic properties of the material vary with pressure, we carried out zero-field-cooled susceptibility measurements at 1.2(1), 3.8(1), 5.2(1), and 8.4(1) kbar on a pelletized polycrystalline sample. At each pressure, the magnetic susceptibility increases on cooling until a broad maximum is reached at the ordering temperature [Fig. 5(a)]. The ordering temperature shifts to higher values as the sample is compressed and is accompanied by a decrease in the maximum susceptibility. At the highest measured pressure, 8.4(1) kbar, $Ni(NCS)_2$ orders at $T_N = 64.6(4)$ K, which is a +19% increase from ambient pressure, giving $Q = +2.3\%$ kbar^{-1} [Fig. 5(b)].

We also carried out isothermal measurements at the same pressure points at 10 K between −7 and +7 T [Fig. 5(c)], which did not show saturation in this field regime, as expected for a bulk antiferromagnet. We found that the maximum magnetization that was measured increased up to 3.8(1) kbar, before decreasing at higher pressures.

D. Magnetic structure

Our bulk magnetic measurements showed a significant enhancement in magnetic ordering temperature; however, to understand the detailed evolution of the magnetic structure, we carried out neutron diffraction measurements on a powder sample (1.2 g) using the high-flux D1b diffractometer at

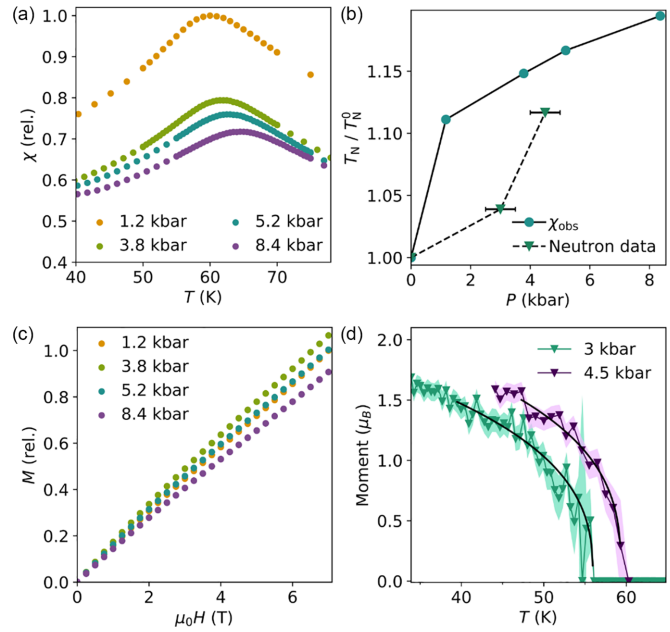

FIG. 5. (a) Magnetic susceptibility measured at 1.2(1), 3.8(1), 5.2(1), and 8.4(1) kbar; the relative susceptibility has been normalized to the maximum susceptibility at 1.2 kbar. (b) Relative change in T_N as a function of pressure derived from susceptibility (circles) and neutron diffraction data (triangles). Error bars related to pressure determination are shown for the neutron data; the error bars are contained within the symbols for the magnetometry data. The ordering temperatures were normalized to the ambient pressure ordering temperature, $T_N^0 = 54$ K. (c) Isothermal magnetization measurements carried out at 10 K plotted between 0 and +7 T, showing the relative magnetization normalized to the maximum magnetization at 1.2 kbar. (d) The magnetic moment determined from Rietveld refinement of the neutron diffraction data (D1b, ILL) at 3 and 4.5 kbar, fitted by a power law, given by Eq. (1) (black line). The shaded regions show the calculated errors of the magnitude of the moment.

the ILL. Neutron diffraction data were collected below the ordering temperatures at 3, 4.5, and 6.7 kbar at the lowest temperatures for each pressure ($P = 3$ kbar, $T = 34$ K; $P = 4.5$ kbar, $T = 44$ K; $P = 6.7$ kbar, $T = 20$ K). In these low-temperature data sets, we observed the appearance of an additional Bragg reflection at 0.54 Å^{-1} at all pressures [Fig. 2(c)] and no other additional reflections, which allowed us to confirm that the propagation vector is $\mathbf{k} = (0, 0, \frac{1}{2})$, identical to that of the ambient pressure material. This propagation vector corresponds to a doubling along the c axis, and we found that of the two maximal magnetic space groups, only the ambient pressure structure C_c2/c was able to reproduce the observed intensity with a reasonable moment size.

We then carried out Rietveld refinements on these datasets in which the magnitude of the nickel moment was fixed to 1.75 μ_B, in accordance with the reported size of the moment at 2 K at ambient pressure [17], due to the paucity of magnetic Bragg peaks. This then allowed for the angle to be refined as the only free magnetic parameter. At all three pressures, the angle of the moment remains broadly unchanged from the ambient structure model, that is, the moment is oriented along the N-Ni-N bond within the ac plane. As the moment direction does not change up to 6.7 kbar or on warming at

ambient pressure [17], for the following magnetic refinements, therefore, we fixed the moment direction to point along the N-Ni-N bonds. This allowed us to refine the size of the magnetic moment as the only free magnetic parameter in the last cycles of the refinement.

Having established that the magnetic ground state remained unchanged, we next looked to understand the nature of the ordering transition. We collected variable temperature data at 3 kbar ($T = 34$–65 K) and 4.5 kbar ($T = 44$–60 K). At 3 kbar, the magnetic moment was refined to $1.68(7)\,\mu_B$ for the lowest-temperature point ($T = 34$ K) and the ordering temperature is found at $T_N = 56.1(5)$ K. At 4.5 kbar, the refined moment is $1.58(7)\,\mu_B$ ($T = 44$ K) and decreases with temperature to $0\,\mu_B$ at $T_N = 58.0(5)$ K. We were able to fit the refined magnetic moments to a power law in the vicinity of the transition,

$$M = A(T_N - T)^{\beta}, \tag{1}$$

where A is a proportionality constant, T_N is the ordering temperature, and β is a critical exponent [Fig. 5(d)]. For the fits, the errors for A, T_N, and β are calculated from the square root of the covariance matrix from the errors of the refined magnetic moment. At 3 kbar, the fitted values were $\beta = 0.36(6)$ and $T_N = 55.9(7)$ K. At 4.5 kbar, the fitted values were $\beta = 0.33(5)$ and $T_N = 59.3(3)$ K. The values of β are in between 0.326 and 0.367, which is expected for a three-dimensional Ising and Heisenberg antiferromagnet [43].

To gain a deeper understanding of the exchange interactions responsible for the magnetic behavior, we carried out DFT calculations on a variety of spin states as a function of pressure. Geometry optimizations, including both atomic positions and cell parameters, were carried out to probe the magnetic ground state at the same pressures as previously explored (0, 5, 10, 20, 50, and 100 kbar), for six high-symmetry configurations (Table 3 of the Supplemental Material [29]), and the resultant energies and enthalpies were calculated using the Hamiltonian $E = \sum_{ij} J_{ij} S_i S_j + E_0$.

We fitted these DFT-derived energies to a Heisenberg collinear spin Hamiltonian to extract three interactions: J_1 along the Ni-S-Ni direction, J_2 along the Ni-S-C-N-Ni direction, and J_3 corresponding the interactions between layers. At ambient pressure, J_1 is large and ferromagnetic, $-43(8)$ K, J_2 is weaker and also ferromagnetic, $-4(4)$ K, and J_3 is zero within error, consistent with the expected ground state (Fig. 6). The large values of the error suggest that the Heisenberg Hamiltonian that we employed is perhaps not appropriate, either due to large single-ion effects or higher-order interactions (e.g., biquadratic interactions). It is likely that up to 50 kbar, the reported ambient antiferromagnetic structure is the most stable configuration. However, we did not find a strong trend in the predicted J values with pressure beyond the error of the calculations since the relative energy differences between selected spin configurations here are less than 1 meV/metal, meaning we are close to the limits of accuracy for these DFT calculations.

IV. DISCUSSION

From our diffraction data, we have calculated the bulk modulus of $Ni(NCS)_2$ to be $B_0 = 170(2)$ kbar, which shows that $Ni(NCS)_2$ is one of the softer van der Waals compounds,

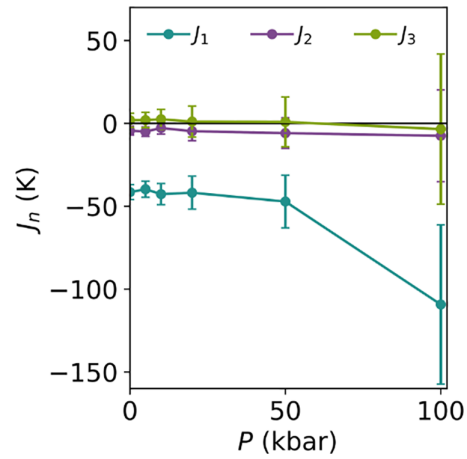

FIG. 6. Calculated enthalpies of the three nearest-neighbor interactions obtained from DFT calculations at ambient, 5, 10, 20, 50, and 100 kbar, where $J > 0$ describes antiferromagnetic interactions and $J < 0$ describes ferromagnetic interactions. The calculated uncertainties associated with fitting to the Heisenberg Hamiltonian are shown with vertical lines.

e.g., for $CrBr_3$, $B_0 = 230$ kbar [44], and for $FePSe_3$, $B_0 = 828$ kbar [11]. High-pressure structural phase transitions are common in layered compounds [10,45,46]; however, our DFT calculations do not provide any evidence of a structural phase transition up to 100 kbar. *Ab initio* structure searches and larger supercell calculations, together with higher-pressure calculations, would allow further exploration of the potential for new $Ni(NCS)_2$ phases. These calculations also suggest that any metallization transition occurs significantly above 100 kbar, compared to NiI_2, $P_c = 190$ kbar [47]; $FeCl_2$, $P_c = 450$ kbar [8]; and $FePS_3$, $P_c \approx 140$ kbar [10].

We can also compare $Ni(NCS)_2$ with other pseudobinary molecular frameworks. Since changing the metal cation species can influence the flexibility of the structure, we focus here on Ni^{2+} frameworks [48]. The three-dimensional $Ni(dca)_2$ [dca = $N(CN)_2$] has a larger bulk modulus, $B_0 = 360$ kbar [49], than $Ni(NCS)_2$. As the ligand length increases, it would be expected that the structure becomes more flexible [50]; however, as $Ni(dca)_2$ is three-dimensionally connected, the resultant bulk modulus is larger than that of layered $Ni(NCS)_2$. The volumetric compressibility provides only a partial picture, as both compounds are anisotropic. The compressibility of $Ni(dca)_2$ along the b and c axes is similar to that of $Ni(NCS)_2$ along the X_2 and X_3 ($b = 11.1$ TPa^{-1} and $c = 24.1$ TPa^{-1}), but $Ni(dca)_2$ shows negative linear compressibility (NLC) in the third (a) direction. The materials have similar ligand arrangements along the a axis, where the nickel ions are bridged by two ligands coordinated in an end-to-end arrangement. In both materials, the hinge ligand-metal-ligand bond angles ω ($\omega = \angle$N-Ni-S and $\angle$N-Ni-N; Fig. 7) decrease: $[\Delta\cos(\frac{\omega}{2})]/P = 0.09\%\,\text{kbar}^{-1}$ (NCS), compared to $[\Delta\cos(\frac{\omega}{2})]/P = 0.16\%\,\text{kbar}^{-1}$ (dca). In $Ni(NCS)_2$, the softer Ni-L bonds mean that there is still contraction in the bond lengths (Ni-N $= -0.12\%\,\text{kbar}^{-1}$ and Ni-S $= -0.18\%\,\text{kbar}^{-1}$). This competition between the two components is likely the cause of the apparent stiffness of the a axis. In contrast, the square-planar $Ni(CN)_2$ is significantly

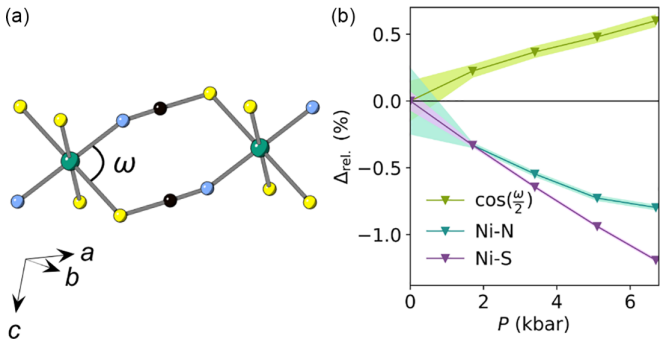

FIG. 7. (a) Nickel ions connected through two NCS ligands, showing the "hinge" angle, ω. Ni = green, N = blue, C = black, S = yellow. (b) Relative change in the bond lengths Ni-N and Ni-S, and the relative change in $\cos(\frac{\omega}{2})$ with pressure. The ambient pressure values were obtained from Ref. [20]. The shaded regions show the errors.

stiffer, $B_0 = 1050$ kbar, perhaps due to the planarity of the structure and linearity of Ni-CN-Ni bonds [51].

Our high-pressure variable-temperature data show that despite being a layered structure, $Ni(NCS)_2$ has near zero thermal expansion along the X_3 direction. In comparison, there is positive thermal expansion along the X_1 and X_2 directions (Fig. 4). Calculating the thermal expansion coefficients from the published ambient pressure data [17] gives values of $\alpha_1 = 26(2)\ \mathrm{MK}^{-1}$, $\alpha_2 = 2.1(9)\ \mathrm{MK}^{-1}$, and $\alpha_3 = -5.9(9)\,\mathrm{MK}^{-1}$. Here, the principal axes are defined as $X_1 = 0.47a + 0.88c$, $X_2 = b$, and $X_3 = -0.56a + 0.83c$ at 100 K. This is rotated slightly in comparison to the high-pressure data (definitions are approximately equal to the directions given in Table I). X_3 exhibits negative thermal expansion, which is uncommon; however, it can be observed in other anisotropic molecular framework compounds [52,53]. These values are comparable to those seen at 6.7 kbar, but the within-layer expansion has decreased. This behavior is not uncommon in layered molecular frameworks and likely reflects the stiffening of the transverse out-of-plane vibrations [52]. Since the ambient pressure structure was measured between 1 and 100 K, and our high-pressure data were measured between 20 and 298 K, direct comparison of coefficients should be done cautiously. Future investigations would be needed for detailed quantitative comparisons.

The most significant change observed on compressing $Ni(NCS)_2$ is the marked increase in magnetic ordering temperature, $Q = +2.3\%\ \mathrm{kbar}^{-1}$. This increase is large compared to other nickel molecular frameworks, such as $Ni(dca)_2$ ($Q = +0.4\%\,\mathrm{kbar}^{-1}$) [54], $NH_4Ni(HCOO)_3$ ($Q = +0.2\%\,\mathrm{kbar}^{-1}$) [55], and $NiCl_2(pym)_2$, pym = pyrimidine ($Q = +1.3\%\,\mathrm{kbar}^{-1}$) [56]. For additional examples, see Refs. [3,4,8,10,11,49,54–65] summarized in the Supplemental Material [29], Fig. 4 and Table 5. The increase of ordering temperatures in these compounds results from both changes in exchange interactions, including the increase in strength of interactions and reduction of frustrating interactions, and the single-ion anisotropy. Our DFT calculations suggest that this compound is not magnetically frustrated, and so the general anticipated enhancement of exchange will be largely reinforcing. The significant uncertainties in the DFT-derived superexchange parameters suggest that higher-level calculations, incorporating single-ion anisotropy and higher-order exchange interactions, might be necessary for a complete understanding of the underlying magnetic Hamiltonian. The interlayer J_3 pathway, through Ni-S$\cdots$S-Ni, significantly decreases in distance and is likely the limiting factor in the ordering temperature.

This shift towards a three-dimensional exchange network can be seen in the critical exponent of the temperature dependence of the staggered magnetic moment. A power-law fit [Eq. (1)] of the Rietveld-refined magnetic moment as a function of temperature at 3 and 4.5 kbar [Fig. 5(d)], gave critical exponents of $\beta = 0.36(6)$ and 0.33(5), comparable to the three-dimensional Heisenberg results ($\beta = 0.367$), whereas fitting to the published ambient pressure data [17] gave $\beta = 0.25(4)$ and $T_N = 60.3(6)$ K. The high-pressure value is consistent with those of three-dimensional molecular framework magnets, e.g., $Mn(dca)_2(pyz)$ (pyz=pyrazine), where $\beta = 0.38$ [66], whereas the ambient pressure exponent is closer to that of other vdW magnets, e.g., $NiCl_2$, $\beta = 0.27$ [67]; and $FeCl_2$, $\beta = 0.29$ [68]. Unfortunately, comparatively large errors (relative to the small energy differences between selected spin configurations) in our DFT-derived superexchange parameters do not allow us to further buttress this picture (Fig. 6). More direct exploration of the changes in the exchange parameters, whether through spectroscopy or other bulk measurements, would be valuable to explore this two-dimensional to three-dimensional crossover.

We find no evidence of any spin rotation with pressure in $Ni(NCS)_2$ up to 6.7 kbar. This is consistent with the behavior of other vdW metal halides, including NiI_2, CoI_2 [47], and $FeCl_2$ [58]. This is perhaps due to strong easy-axis single-ion anisotropy in this material [23,69].

V. CONCLUSION

We have investigated the effects of pressure on the structure and magnetism of the van der Waals framework $Ni(NCS)_2$. X-ray and neutron powder diffraction data reveal strongly anisotropic strain, with the interlayer direction being an order of magnitude more compressible than the a direction. Low-temperature neutron diffraction measurements combined with susceptibility data show there is a significant increase in the magnetic ordering temperature with pressure driven by the reduction of interlayer separation. This work has explored the use of a thiocyanate framework as a source of flexibility to enhance the changes in the magnetic properties of a van der Waals material. It suggests that further molecular framework magnets hold potential to show marked responses to compression. Following this work, it would also be worthwhile to explore the monolayer limits of $Ni(NCS)_2$ under pressure to observe if more drastic changes to the magnetic structure can be obtained for a few-layer molecular framework.

The raw data sets are available at Refs. [70,71].

ACKNOWLEDGMENTS

M.G. acknowledges the Institut Laue Langevin (ILL, France) Graduate School for provision of a studentship. M.J.C. acknowledges the School of Chemistry,

University of Nottingham for support from Hobday bequest. We acknowledge the ILL for beam time under Proposal No. 5-24-660. S.L. acknowledges the use of the Sulis supercomputer through the HPC Midlands+ Consortium, and the ARCHER2 supercomputer through membership of the UK's HPC Materials Chemistry Consortium, which are funded by EPSRC Grants No. EP/T022108/1 and No. EP/R029431/1, respectively. The MPMS measurements were carried out using the Advanced Materials Characterisation Suite in the Maxwell Centre, University of Cambridge, funded by EPSRC Strategic Equipment Grant No. EP1M000524/1. We acknowledge Diamond Light Source (UK) for beam time on beamline I15 under Proposal No. CY30815-2.

M.G. and M.J.C. synthesized the samples. M.J.C., D.M.J., C.L., and S.S.S. carried out the magnetometry measurements and analysis. A.B.C., M.G., O.F., L.C.D., and M.J.C. carried out the neutron diffraction experiment and analysis. S.L. carried out the density functional theory calculations. J.P., E.M., S.A.H., S.M.K., G.K., and D.D. carried out the x-ray diffraction measurements. M.J.C., M.G., and L.C.D. performed the analysis of the x-ray diffraction data. M.G., L.C.D., and M.J.C. wrote the paper with contributions from all authors.

[1] D. L. Cortie, G. L. Causer, K. C. Rule, H. Fritzsche, W. Kreuzpaintner, and F. Klose, Two-dimensional magnets: Forgotten history and recent progress towards spintronic applications. Advanced functional materials, Adv. Funct. Mater. **30**, 1901414 (2020).

[2] T. Song, Z. Fei, M. Yankowitz, Z. Lin, Q. Jiang, K. Hwangbo, Q. Zhang, B. Sun, T. Taniguchi, K. Watanabe, M. A. McGuire, D. Graf, T. Cao, J.-H. Chu, D. H. Cobden, C. R. Dean, D. Xiao, and X. Xu, Switching 2D magnetic states via pressure tuning of layer stacking, Nat. Mater. **18**, 1298 (2019).

[3] W. M. Xu and M. P. Pasternak, Magnetism in $FeCl_2$ at high pressures, in *Mössbauer Spectroscopy*, edited by P. Gütlich, B. W. Fitzsimmons, R. Rüffer, and H. Spiering (Springer, Dordrecht, 2003), pp. 175–181.

[4] M. P. Pasternak, R. D. Taylor, A. Chen, C. Meade, L. M. Falicov, A. Giesekus, R. Jeanloz, and P. Y. Yu, Pressure-induced metallization and the collapse of the magnetic state in the antiferromagnetic insulator NiI_2, Phys. Rev. Lett. **65**, 790 (1990).

[5] J. Kapeghian, D. Amoroso, C. A. Occhialini, L. G. P. Martins, Q. Song, J. S. Smith, J. J. Sanchez, J. Kong, R. Comin, P. Barone, B. Dupé, M. J. Verstraete, and A. S. Botana, Effects of pressure on the electronic and magnetic properties of bulk NiI_2, arXiv:2306.04729.

[6] C. A. Occhialini, L. G. P. Martins, Q. Song, J. S. Smith, J. Kapeghian, D. Amoroso, J. J. Sanchez, P. Barone, B. Dupé, M. j. Verstraete, J. Kong, A. S. Botana, and R. Comin, Signatures of pressure-enhanced helimagnetic order in van der Waals multiferroic NiI_2, arXiv:2306.11720.

[7] G. K. Rozenberg, W. Xu, and M. P. Pasternak, The Mott insulators at extreme conditions; structural consequences of pressure-induced electronic transitions, Z. Kristallogr. Crystal. Mater. **229**, 210 (2014).

[8] G. K. Rozenberg, M. P. Pasternak, P. Gorodetsky, W. M. Xu, L. S. Dubrovinsky, T. Le Bihan, and R. D. Taylor, Pressure-induced structural, electronic, and magnetic phase transitions in $FeCl_2$ studied by x-ray diffraction and resistivity measurements, Phys. Rev. B **79**, 214105 (2009).

[9] M. P. Pasternak, W. M. Xu, G. K. Rozenberg, R. D. Taylor, G. R. Hearne, and E. Sterer, Pressure-induced magnetic and electronic transitions in the layered Mott insulator FeI_2, Phys. Rev. B **65**, 035106 (2001).

[10] M. J. Coak, D. M. Jarvis, H. Hamidov, A. R. Wildes, J. A. M. Paddison, C. Liu, C. R. S. Haines, N. T. Dang, S. E. Kichanov, B. N. Savenko, S. Lee, M. Kratochvílová, S. Klotz, T. C. Hansen, D. P. Kozlenko, J.-G. Park, and S. S. Saxena, Emergent magnetic phases in pressure-tuned van der Waals antiferromagnet $FePS_3$, Phys. Rev. X **11**, 011024 (2021).

[11] Y. Wang, J. Ying, Z. Zhou, J. Sun, T. Wen, Y. Zhou, N. Li, Q. Zhang, F. Han, Y. Xiao, P. Chow, W. Yang, V. V. Struzhkin, Y. Zhao, and H.-k. Mao, Emergent superconductivity in an iron-based honeycomb lattice initiated by pressure-driven spin-crossover, Nat. Commun. **9**, 1914 (2018).

[12] P. Serra-Crespo, A. Dikhtiarenko, E. Stavitski, J. Juan-Alcañiz, F. Kapteijn, F.-X. Coudert, and J. Gascon, Experimental evidence of negative linear compressibility in the MIL-53 metal–organic framework family, CrystEngComm **17**, 276 (2015).

[13] H. Wu, T. Yildirim, and W. Zhou, Exceptional mechanical stability of highly porous zirconium metal–organic framework UiO-66 and its important implications, J. Phys. Chem. Lett. **4**, 925 (2013).

[14] W. Kaneko, M. Mito, S. Kitagawa, and M. Ohba, Interpenetrated three-dimensional $Mn^{II}M^{III}$ ferrimagnets, $[Mn(4\text{-dmap})_4]_3[M(CN)_6]_2.10\ H_2O$ (M=Cr, Mn): Structures, magnetic properties, and pressure-responsive magnetic modulation, Chem. Europ. J. **14**, 3481 (2008).

[15] W. Shum, J.-H. Her, P. Stephens, Y. Lee, and J. Miller, Observation of the pressure dependent reversible enhancement of T_c and loss of the anomalous constricted hysteresis for $[Ru_2(O_2CMe)_4]_3[Cr(CN)_6]$, Adv. Mater. **19**, 2910 (2007).

[16] J. López-Cabrelles, S. Mañas-Valero, I. J. Vitórica-Yrezábal, P. J. Bereciartua, J. A. Rodríguez-Velamazán, J. C. Waerenborgh, B. J. C. Vieira, D. Davidovikj, P. G. Steeneken, H. S. J. Van Der Zant, G. Mínguez Espallargas, and E. Coronado, Isoreticular two-dimensional magnetic coordination polymers prepared through pre-synthetic ligand functionalization, Nat. Chem. **10**, 1001 (2018).

[17] E. N. Bassey, J. A. M. Paddison, E. N. Keyzer, J. Lee, P. Manuel, I. da Silva, S. E. Dutton, C. P. Grey, and M. J. Cliffe, Strengthening the magnetic interactions in pseudobinary first-row transition metal thiocyanates, $M(NCS)_2$, Inorg. Chem. **59**, 11627 (2020).

[18] P. Perlepe, I. Oyarzabal, A. Mailman, M. Yquel, M. Platunov, I. Dovgaliuk, M. Rouzières, P. Négrier, D. Mondieig, E. A. Suturina, M. A. Dourges, S. Bonhommeau, R. A. Musgrave, K. S. Pedersen, D. Chernyshov, F. Wilhelm, A. Rogalev, C. Mathonière, and R. Clérac, Metal-organic magnets with large coercivity and ordering temperatures up to 242°C, Science **370**, 587 (2020).

[19] E. Shurdha, S. H. Lapidus, P. W. Stephens, C. E. Moore, A. L. Rheingold, and J. S. Miller, Extended network thiocyanate- and tetracyanoethanide-based first-row transition metal complexes, Inorg. Chem. **51**, 9655 (2012).

[20] E. Dubler, A. Reller, and H. R. Oswald, Intermediates in thermal decomposition of nickel(II) complexes: The crystal structures of $Ni(SCN)_2(NH_3)_2$ and $Ni(SCN)_2$, Z. Kristallogr. **161**, 265 (1982).

[21] M. J. Cliffe, J. Lee, J. A. M. Paddison, S. Schott, P. Mukherjee, M. W. Gaultois, P. Manuel, H. Sirringhaus, S. E. Dutton, and C. P. Grey, Low-dimensional quantum magnetism in $Cu(NCS)_2$: A molecular framework material, Phys. Rev. B **97**, 144421 (2018).

[22] A. Adam, D. Billerey, C. Terrier, R. Mainard, L. Regnault, J. Rossat-Mignod, and P. Mériel, Neutron diffraction study of the commensurate and incommensurate magnetic structures of $NiBr_2$, Solid State Commun. **35**, 1 (1980).

[23] Y. Wu, W. Sun, S. Liu, B. Wang, C. Liu, H. Yin, and Z. Cheng, $Ni(NCS)_2$ monolayer: a robust bipolar magnetic semiconductor, Nanoscale **13**, 16564 (2021).

[24] A. Eiling and J. S. Schilling, Pressure and temperature dependence of electrical resistivity of Pb and Sn from 1-300K and 0-10 GPa-use as continuous resistive pressure monitor accurate over wide temperature range; superconductivity under pressure in Pb, Sn and In, J. Phys. F **11**, 623 (1981).

[25] S. Grimme, J. Antony, S. Ehrlich, and H. Krieg, A consistent and accurate ab initio parametrization of density functional dispersion correction (DFT-D) for the 94 elements H-Pu, J. Chem. Phys. **132**, 154104 (2010).

[26] G. Kresse and J. Furthmüller, Efficient iterative schemes for ab initio total-energy calculations using a plane-wave basis set, Phys. Rev. B **54**, 11169 (1996).

[27] W. E. Pickett, S. C. Erwin, and E. C. Ethridge, Reformulation of the LDA + U method for a local-orbital basis, Phys. Rev. B **58**, 1201 (1998).

[28] F. Zhou, M. Cococcioni, C. A. Marianetti, D. Morgan, and G. Ceder, First-principles prediction of redox potentials in transition-metal compounds with LDA + U, Phys. Rev. B **70**, 235121 (2004).

[29] See Supplemental Material at http://link.aps.org/supplemental/10.1103/PhysRevB.108.144439 for density functional theory spin configurations and results, and unit cell parameters for X-ray and neutron refinements.

[30] J. P. Perdew, K. Burke, and M. Ernzerhof, Generalized Gradient Approximation Made Simple, Phys. Rev. Lett. **77**, 3865 (1996).

[31] P. E. Blöchl, Projector augmented-wave method, Phys. Rev. B **50**, 17953 (1994).

[32] D. Hobbs, G. Kresse, and J. Hafner, Fully unconstrained non-collinear magnetism within the projector augmented wave method, Phys. Rev. B **62**, 11556 (2000).

[33] N. J. Brooks, B. L. L. E. Gauthe, N. J. Terrill, S. E. Rogers, R. H. Templer, O. Ces, and J. M. Seddon, Automated high pressure cell for pressure jump x-ray diffraction, Rev. Sci. Instrum. **81**, 064103 (2010).

[34] J. Filik, A. W. Ashton, P. C. Y. Chang, P. A. Chater, S. J. Day, M. Drakopoulos, M. W. Gerring, M. L. Hart, O. V. Magdysyuk, S. Michalik, A. Smith, C. C. Tang, N. J. Terrill, M. T. Wharmby, and H. Wilhelm, Processing two-dimensional X-ray diffraction and small-angle scattering data in DAWN 2, J. Appl. Crystallogr. **50**, 959 (2017).

[35] J. Rodríguez-Carvajal, Recent advances in magnetic structure determination by neutron powder diffraction, Physica B: Condens. Matter **192**, 55 (1993).

[36] M. J. Cliffe and A. L. Goodwin, PASCal : a principal axis strain calculator for thermal expansion and compressibility determination, J. Appl. Crystallogr. **45**, 1321 (2012).

[37] A. Hewat, A New High Resolution Neutron Powder Diffractometer at Ill Grenoble, Mater. Sci. Forum **9**, 69 (1986).

[38] P. Mutti, F. Cecillon, A. Elaazzouzi, Y. Le Goc, J. Locatelli, H. Ortiz, and J. Ratel, Nomad more than a simple sequencer (unpublished).

[39] I. P. Orench, J. F. Clergeau, S. Martínez, M. Olmos, O. Fabelo, and J. Campo, The new powder diffractometer D1B of the Institut Laue Langevin, J. Phys.: Conf. Ser. **549**, 012003 (2014).

[40] F. Birch, Finite elastic strain of cubic crystals, Phys. Rev. **71**, 809 (1947).

[41] L. Tassini, F. Gorelli, and L. Ulivi, High temperature structures and orientational disorder in compressed solid nitrogen, J. Chem. Phys. **122**, 074701 (2005).

[42] F. A. Gorelli, M. Santoro, L. Ulivi, and M. Hanfland, Crystal structure of solid oxygen at high pressure and low temperature, Phys. Rev. B **65**, 172106 (2002).

[43] S. Blundell, *Magnetism in Condensed Matter*, Oxford Master Series in Condensed Matter Physics (Oxford University Press, Oxford, 2001).

[44] A. S. Ahmad, Y. Liang, M. Dong, X. Zhou, L. Fang, Y. Xia, J. Dai, X. Yan, X. Yu, J. Dai, G.-j. Zhang, W. Zhang, Y. Zhao, and S. Wang, Pressure-driven switching of magnetism in layered $CrCl_3$, Nanoscale **12**, 22935 (2020).

[45] C. S. R. Haines, M. J. Coak, A. R. Wildes, G. I. Lampronti, C. Liu, P. Nahai-Williamson, H. Hamidov, D. Daisenberger, and S. S. Saxena, Pressure-induced electronic and structural phase evolution in the van der Waals compound $FePS_3$, Phys. Rev. Lett. **121**, 266801 (2018).

[46] X. Wang, X. Chen, Y. Zhou, C. Park, C. An, Y. Zhou, R. Zhang, C. Gu, W. Yang, and Z. Yang, Pressure-induced iso-structural phase transition and metallization in WSe_2, Sci. Rep. **7**, 46694 (2017).

[47] M. P. Pasternak, R. D. Taylor, and R. Jeanloz, Pressure-induced Mott transition in transition-metal iodides (invited), J. Appl. Phys. **70**, 5956 (1991).

[48] S. Grover, S. Burger, K. T. Butler, K. Hemmer, P. Vervoorts, G. Kieslich, and R. Grau-Crespo, Tuning the mechanical properties of dicyanamide-based molecular perovskites, CrystEngComm **25**, 3439 (2023).

[49] X. Fan, T. Yan, Q. Wang, J. Zheng, Z. Ma, and Z. Xue, Negative linear compressibility of nickel dicyanamide, Chem. Lett. **48**, 1375 (2019).

[50] S. Dissegna, P. Vervoorts, C. L. Hobday, T. Düren, D. Daisenberger, A. J. Smith, R. A. Fischer, and G. Kieslich, Tuning the mechanical response of metal–organic frameworks by defect engineering, J. Am. Chem. Soc. **140**, 11581 (2018).

[51] S. K. Mishra, R. Mittal, M. Zbiri, R. Rao, P. Goel, S. J. Hibble, A. M. Chippindale, T. Hansen, H. Schober, and S. L. Chaplot, New insights into the compressibility and high-pressure stability of $Ni(CN)_2$: A combined study of neutron diffraction, Raman spectroscopy, and inelastic neutron scattering, J. Phys.: Condens. Matter **28**, 045402 (2016).

[52] S. A. Hodgson, J. Adamson, S. J. Hunt, M. J. Cliffe, A. B. Cairns, A. L. Thompson, M. G. Tucker, N. P. Funnell, and

A. L. Goodwin, Negative area compressibility in silver(I) tricyanomethanide, Chem. Commun. **50**, 5264 (2014).

[53] I. E. Collings, J. A. Hill, A. B. Cairns, R. I. Cooper, A. L. Thompson, J. E. Parker, C. C. Tang, and A. L. Goodwin, Compositional dependence of anomalous thermal expansion in perovskite-like ABX_3 formates, Dalton Trans. **45**, 4169 (2016).

[54] C. J. Nuttall, T. Takenobu, Y. Iwasa, and M. Kurmoo, Pressure dependence of the magnetization of $M^{II}(N(CN)_2)_2$: Mechanism for the long range magnetic ordering, Mol. Cryst. Liq. Cryst. Sci. Technol., Sect. A **343**, 227 (2000).

[55] I. E. Collings, R. S. Manna, A. A. Tsirlin, M. Bykov, E. Bykova, M. Hanfland, P. Gegenwart, S. van Smaalen, L. Dubrovinsky, and N. Dubrovinskaia, Pressure dependence of spin canting in ammonium metal formate antiferromagnets, Phys. Chem. Chem. Phys. **20**, 24465 (2018).

[56] J. Kreitlow, D. Menzel, A. U. B. Wolter, J. Schoenes, S. Süllow, R. Feyerherm, and K. Doll, Pressure dependence of $C_4N_2H_4$-mediated superexchange in $XCl_2(C_4N_2H_4)_2$ (X = Fe, Co, Ni), Phys. Rev. B **72**, 134418 (2005).

[57] O. Lis, D. Kozlenko, S. Kichanov, E. Lukin, I. Zel, and B. Savenko, Structural, magnetic and vibrational properties of van der Waals ferromagnet $CrBr_3$ at high pressure, Materials **16**, 454 (2023).

[58] C. Vettier and W. B. Yelon, Magnetic properties of $FeCl_2$ at high pressure, Phys. Rev. B **11**, 4700 (1975).

[59] C. Zhang, Y. Gu, L. Wang, L.-L. Huang, Y. Fu, C. Liu, S. Wang, H. Su, J.-W. Mei, X. Zou, and J.-F. Dai, Pressure-enhanced ferromagnetism in layered $CrSiTe_3$ flakes, Nano Lett. **21**, 7946 (2021).

[60] K. Xu, Z. Yu, W. Xia, M. Xu, X. Mai, L. Wang, Y. Guo, X. Miao, and M. Xu, Unique 2D–3D structure transformations in trichalcogenide $CrSiTe_3$ under high pressure, J. Phys. Chem. C **124**, 15600 (2020).

[61] A. A. Yakovenko, K. W. Chapman, and G. J. Halder, Pressure-induced structural phase transformation in cobalt(II) dicyanamide, Acta Crystallogr. Sect. B Structur. Sci. Crystal Engineer. Mater. **71**, 252 (2015).

[62] I. E. Collings, M. Bykov, E. Bykova, M. G. Tucker, S. Petitgirard, M. Hanfland, K. Glazyrin, S. Van Smaalen, A. L. Goodwin, L. Dubrovinsky, and N. Dubrovinskaia, Structural distortions in the high-pressure polar phases of ammonium metal formates, CrystEngComm **18**, 8849 (2016).

[63] A. Clune, N. Harms, K. R. O'Neal, K. Hughey, K. A. Smith, D. Obeysekera, J. Haddock, N. S. Dalal, J. Yang, Z. Liu, and J. L. Musfeldt, Developing the pressure-temperature-magnetic field phase diagram of multiferroic $[(CH_3)_2NH_2]Mn(HCOO)_3$, Inorg. Chem. **59**, 10083 (2020).

[64] I. E. Collings, M. Bykov, E. Bykova, M. Hanfland, S. Van Smaalen, L. Dubrovinsky, and N. Dubrovinskaia, Disorder-order transitions in the perovskite metal-organic frameworks $[(CH_3)_2NH_2][M(HCOO)_3]$ at high pressure, CrystEngComm **20**, 3512 (2018).

[65] A. Wolter, H.-H. Klauss, F. Litterst, T. Burghardt, A. Eichler, R. Feyerherm, and S. Süllow, A pressure study of the antiferromagnetic phase of $FePM_2Cl_2$ (PM=pyrimidine), Polyhedron **22**, 2139 (2003).

[66] J. L. Manson, Q.-z. Huang, J. W. Lynn, H.-J. Koo, M.-H. Whangbo, R. Bateman, T. Otsuka, N. Wada, D. N. Argyriou, and J. S. Miller, Long-range magnetic order in $Mn[N(CN)_2]_2(pyz)$ {pyz = pyrazine}. Susceptibility, magnetization, specific heat, and neutron diffraction measurements and electronic structure calculations, J. Am. Chem. Soc. **123**, 162 (2001).

[67] P. A. Lindgard, R. J. Birgeneau, H. J. Guggenheim, and J. Als-Nielsen, Spin-wave dispersion and sublattice magnetization in $NiCl_2$, J. Phys. C **8**, 1059 (1975).

[68] W. B. Yelon and R. J. Birgeneau, Magnetic properties of $FeCl_2$ in zero Field. II. Long-range order, Phys. Rev. B **5**, 2615 (1972).

[69] G. C. DeFotis, K. D. Dell, D. J. Krovich, and W. W. Brubaker, Antiferromagnetism of $Ni(SCN)_2$, J. Appl. Phys. **73**, 5386 (1993).

[70] See https://doi.ill.fr/10.5291/ILL-DATA.5-24-660 for the raw data sets.

[71] See http://doi.org/10.17639/nott.7336 for all raw data sets.